CHAPTER IV

Wave Equation Velocity Estimation

4.1. Introduction.

The acoustic wave equation has been successfully applied to the migration problem in reflection seismology. For the velocity estimation problem, however, the wave equation has received limited attention. Wave equation methods have the important attribute of linearity, a property not found in commonly used ray tracing techniques. In this chapter our goal is to define a *velocity spectrum* of CMP gathers using wave equation techniques.

We require the velocity spectrum to have two fundamental properties. 1) It must be a space where energy from different events is a local function of velocity. 2) The space must be defined by invertible transformations. Two other desirable properties are resolution and accuracy.

Ray methods are commonly used to estimate velocity. Their application results in nonlinear transformations on the data. An alternative method of velocity estimation is the *linear moveout method*. An important and elegant feature of this method is that it follows directly from the Snell midpoint coordinate transformation. This method is the most natural choice for implementation with the wave equation.

The linear moveout method estimates velocity using the lateral component of a reference Snell wavefront. We can measure either RMS or interval velocities directly in the data. In a stratified earth, with reflectors coinciding with velocity discontinuities, interval velocity can be measured at any angle, no geometric

approximations need to be done. RMS velocity estimates as defined with Dix's equation can also be determined. With this method we can use wide angle reflections for direct interval velocity estimation. When there are continuous velocity variations between reflectors, reflection traveltime data alone cannot resolve uniquely for the velocity function. The problem is underdetermined. Snell coordinates can then be used to decide when velocity inhomogeneities between reflectors are not negligible.

The LMO method does not define a suitable velocity space. Adding an imaging step, however, makes energy become a local function of velocity. Imaged data in Snell midpoint coordinates will constitute our definition of the linear velocity spectrum. Given that imaging will be needed to transform to our velocity space, we describe three methods to image CMP gathers in Snell midpoint coordinates. First, the phase shift method, which is particularly useful to study downward continuation problems. Second is Stolt's method, which is the fastest and can be complemented with a hyperbolic deformation. (Chapter III). And last, finite difference in (h, τ, ω) space, which allows us to use $v(h,\tau)$ in the downward continuation and do stepout filtering concurrent with imaging. Snell midpoint coordinates enable us to use low order wave equation operators for wide propagation angles. This and the insensitivity of the fifteen degree equation to the background velocity, makes the finite difference method the preferred choice to obtain the velocity spectrum.

The wave equation velocity spectrum can also be used in applications requiring model spaces with linearity and locality properties.

4.2. Ray methods in velocity estimation.

Ray methods can be applied in several domains. In this section only methods in the (h, τ, t) domain will be considered.

All ray tracing techniques for velocity estimation are based on the asymptotic high frequency approximate solution of the wave equation. In a flat earth, travel-time as function of offset for the nth arrival is given by

$$t_n^2(h) \approx t_{0,n}^2 + \frac{4h^2}{v_{RMS,n}^2} + O(h^4) \tag{2.1}$$

where h is half offset, t_0 the vertical traveltime and v_{RMS} the Root Mean Square velocity.

Green (1938) was the first to use this equation to estimate velocity. Plotting $4h^2$ vs t^2 gives straight lines with intercept $t_{0,n}^2$ and slope $1/v_{RMS,n}^2$. To find interval velocities, Dix (1955) derived a relationship using v_{RMS}

$$v_n^2 = \frac{v_{RMS,n}^2 \sum\limits_1^n \Delta t_{0,i} - v_{RMS,n-1}^2 \sum\limits_1^{n-1} \Delta t_{0,i}}{\Delta t_{0,n}} \tag{2.2}$$

This equation is widely used. Hajnal and Serada (1981) give a quantitative discussion of errors in interval velocities computed from Dix's equation. In particular, interval velocity estimates amplify RMS velocity errors, and are oversensitive to errors in the normal incidence traveltime estimates.

LePichon et al (1968) proposes a least—square fit to equation (2.1). His approach is convenient whenever arrival times for particular events can be picked out automatically. Unfortunately, automatic picking is unreliable in low amplitude signal environments. The method is limited by the signal—to—noise ratio of the data.

The most widely accepted method for defining velocity spectrum is Taner and Koehler's (1969) technique. They use equation (2.1) to apply a correction for residual travel time with offset, (NMO correction):
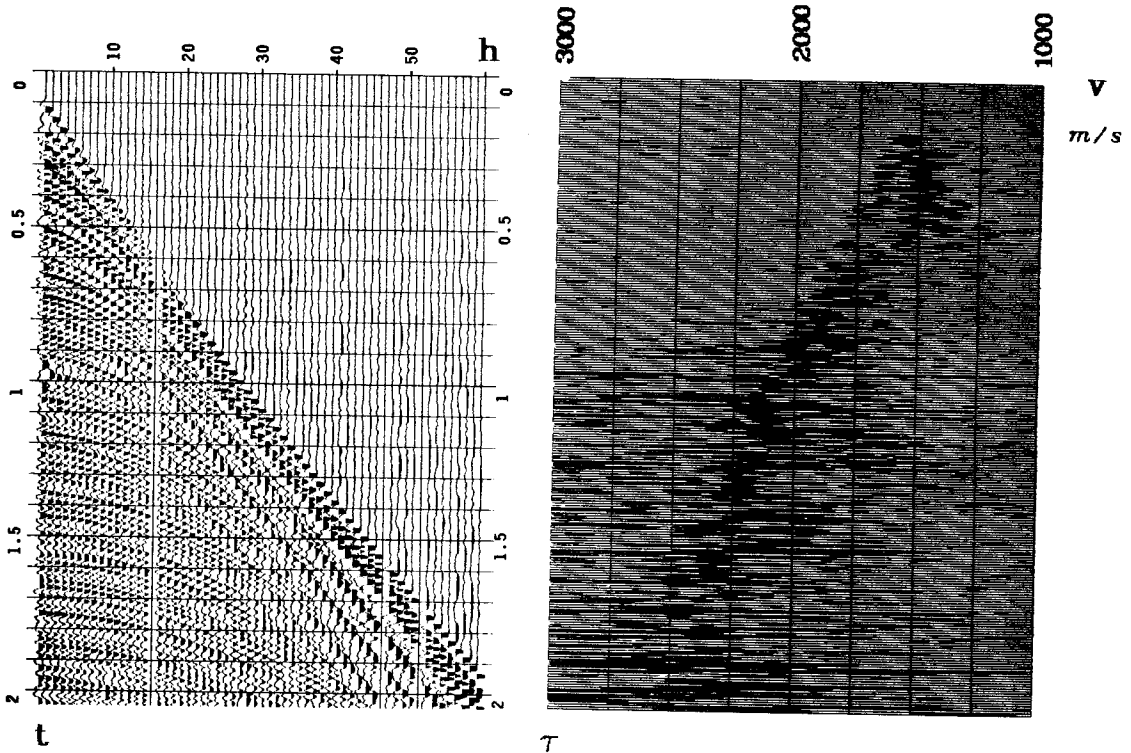
FIGURE 2.1. Hyperbolic velocity spectrum. (a) CMP gather. (b) Hyperbolic velocity spectrum. Only the 30 near offsets were used.

$$t_n(h) - t_{0,n} \equiv \Delta t_n(h) \approx \frac{h^2}{2v_{RMS,n}^2 t_0} \tag{2.3}$$

After NMO, first arrival traveltimes should be independent of offset (approximately if the velocity is not constant). The correction is applied for a trial set of velocities. For display some semblance measure can be used (Neidell and Taner, 1971; Taner and Koehler, 1968). Figure (2.1) is an example of this technique. Energy has to be kept to small propagation angles so all assumed approximations are valid. The method cannot use wide—angle velocity—sensitive energy to improve interval velocity estimates.

May and Straley (1979), include the fourth order term in equation (2.1). This term gives a first order correction to non—hyperbolicity. The truncated series needs to be orthogonalized before estimating its coefficients. Since there

are three coefficients, (zero, second and fourth order), a coherence search needs to be done in 3–D space. They suggest two searches over 2–D planes, implying hyperbolic assumption in one plane. This method is particularly useful as a processing tool, to improve the NMO correction with better stacking velocities.

The ray methods discussed above have the advantage of insensitivity to aliasing. However, they have several important restrictions. First, they are approximations dependent on angle. Error increases with offset where the data is most sensitive to velocity. Second, ray methods are non–linear; and third, their resolution is limited by cable truncations and refractions.

4.3. Imaging CMP gathers in Snell midpoint coordinates.

In chapter (I) we learned that slant wave propagation preserves the velocity information of the data at any depth. Slant downward continuation and imaging does not alter the velocity information of the data. In this section we describe imaging CMP gathers in Snell midpoint coordinates. Given a fixed reference Snell wave, imaging localizes energy to the neighborhood of its corresponding arrival offset.

The double square root equation in Snell midpoint coordinates under the stratified flat reflectors assumption ($Y = 0$), is given by (figure 3.1)

$$T \equiv \frac{k_\tau}{\omega} = 1 - \frac{p_0 v}{1 - p_0^2 v^2} H - \left[1 - \frac{2 p_0 v H + H^2}{1 - p_0^2 v^2} \right]^{1/2} \tag{3.1}$$

$$H = \frac{k_h v}{2 \omega}$$

To image CMP gathers, first we need to put the data from field coordinates $(s, g, t, z=0)$ into Snell midpoint coordinates $(h, y, \tau=0, t')$. The operator (3.1) is defined in the $\omega-k$ domain, so we need to Fourier transform the data
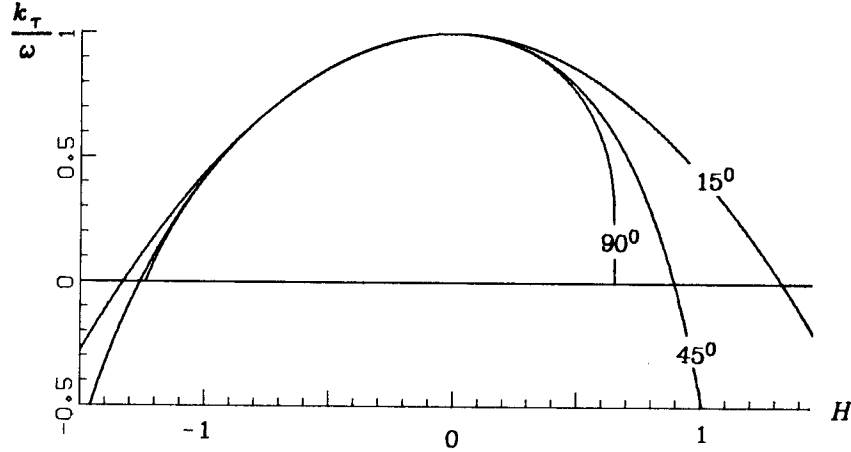
Dispersion relation

FIGURE 3.1. Slant dispersion relation. Square root equation and approximations. Snell midpoint coordinates. $Y = 0, p_0 v = 0.3$

$f(y, h, \tau = 0, t')$. Omitting the y dependence gives

$$F(k_h, \tau = 0, \omega) = \int\int_{-\infty}^{\infty} f(h, \tau = 0, t') \, e^{-ik_h h + i\omega t'} \, dh \, dt' \tag{3.2}$$

using equation (3.1) the data at any time—depth τ is given by

$$F(k_h, \tau, \omega) = F(k_h, \tau = 0, \omega) \exp\left\{ i \int_0^\tau T(\xi) \, \omega \, d\xi \right\} \tag{3.3}$$

Fourier transforming back to (h, τ, t') space

$$f(h, \tau, t') = \frac{1}{4\pi^2} \int\int_{-\infty}^{\infty} F(k_h, \tau = 0, \omega) \exp\left\{ i \int_0^\tau T(\xi) \, \omega \, d\xi + ik_h h - i\omega t' \right\} dk_h \, d\omega \tag{3.4}$$

It can be checked that when $H = 0$, that is, when we are looking at energy that was propagated with initial takeoff angle $\vartheta_0 = \sin^{-1}(p_0 v_{z=0})$, equation (3.1)

becomes $T = 0$. Then equation (3.3) is a *null* operator. This implies that energy propagating with fixed $p = p_0$ will not be moved by the operator T. This property enables velocity estimation at any depth, consequently with the image of the data itself.

To find the image point we need to insert into equation (3.4) an imaging condition. This condition tell us when the wavefield is an image of the reflectivity. This should happen when we have extrapolated the data to $t = 0$. At this point the energy was reflecting from a given interface. At the reflector the positions of the shot and geophone coordinates should be coincident $s = g$. These imaging conditions translate to $t' = \tau$ in the Snell coordinate system. Substitution into equation (3.4) gives

$$f(h,\tau,t'=\tau) = \frac{1}{2\pi} \int\limits_{-\infty}^{\infty}\!\!\int F(k_h,\tau=0,\omega) \exp\left\{ i \int\limits_{0}^{\tau} \omega\,(T(\xi)-1)\,d\xi + ik_h h \right\} dk_h\,d\omega$$

$$(3.5)$$

This equation is what we need to image CMP gathers in Snell midpoint coordinates.

Example. Wavefield extrapolation in Snell midpoint coordinates can be illustrated with downward continuation movies. Figures (3.2) and (3.3) show some of the panels calculated for this purpose.

Figure (3.2) is the $p_0 = 0$ case. Downward continuation was done using the phase shift method. Velocity was $v = 1500\ m/s$ with constant τ—steps. As expected, as downward continuation proceeds, energy migrates toward zero—offsets. Past the depth of the reflectors, energy diffracts toward far and negative offsets. Aliased energy (in refractions area) moves in the wrong direction. To image the data, the imaging principle requires collection of energy that is
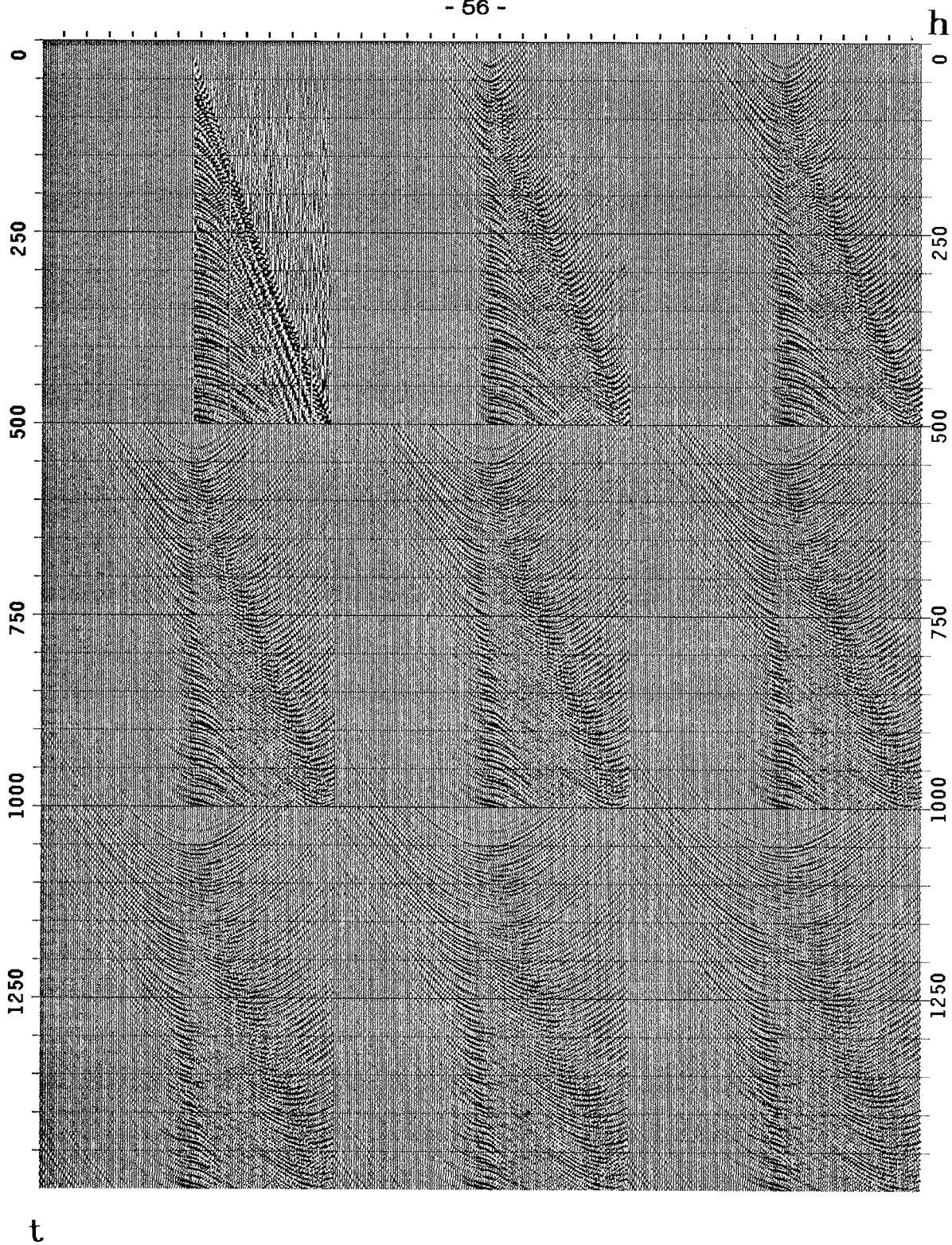
h

t

FIGURE 3.2. Downward continuation. $p_0 = 0$.

h

t

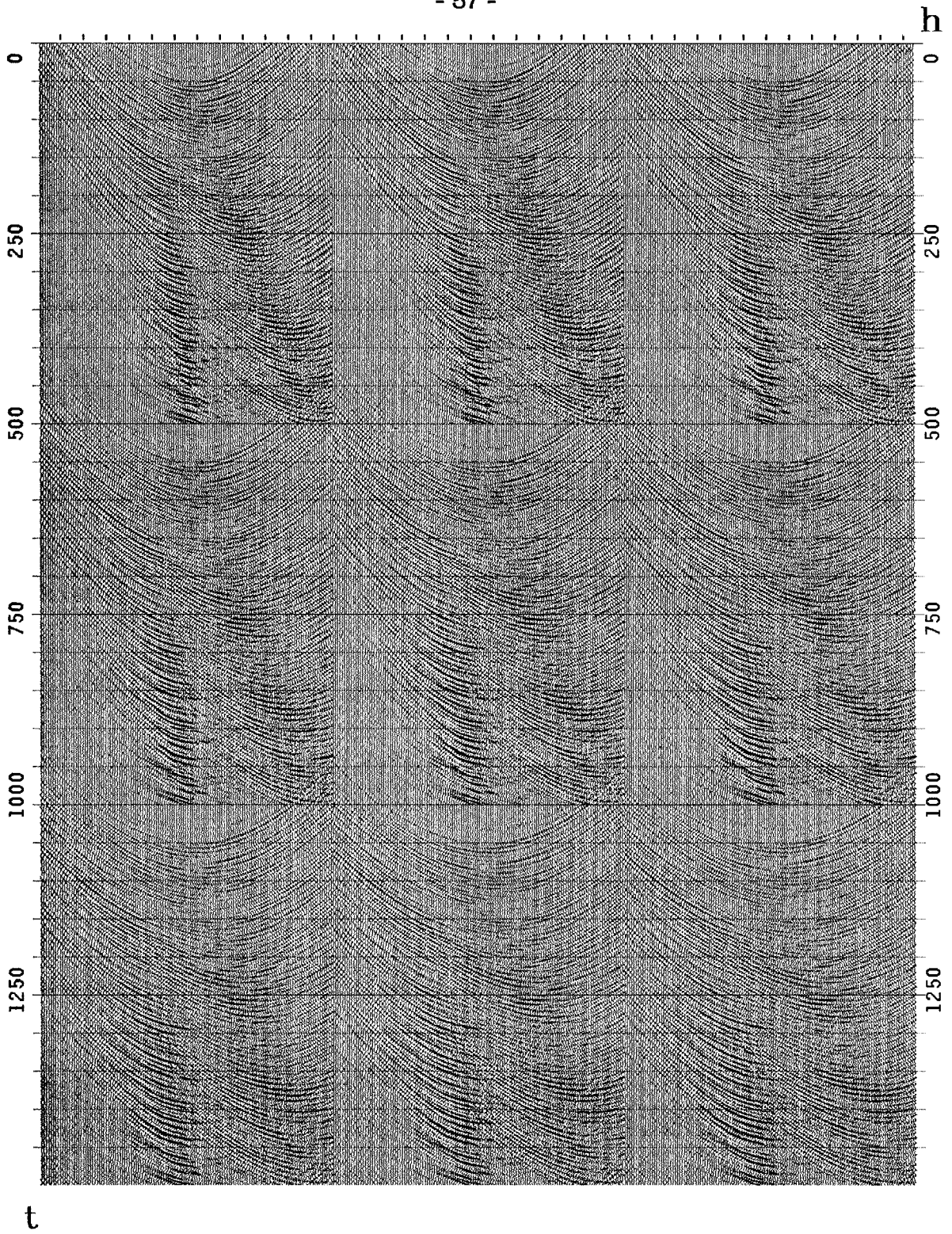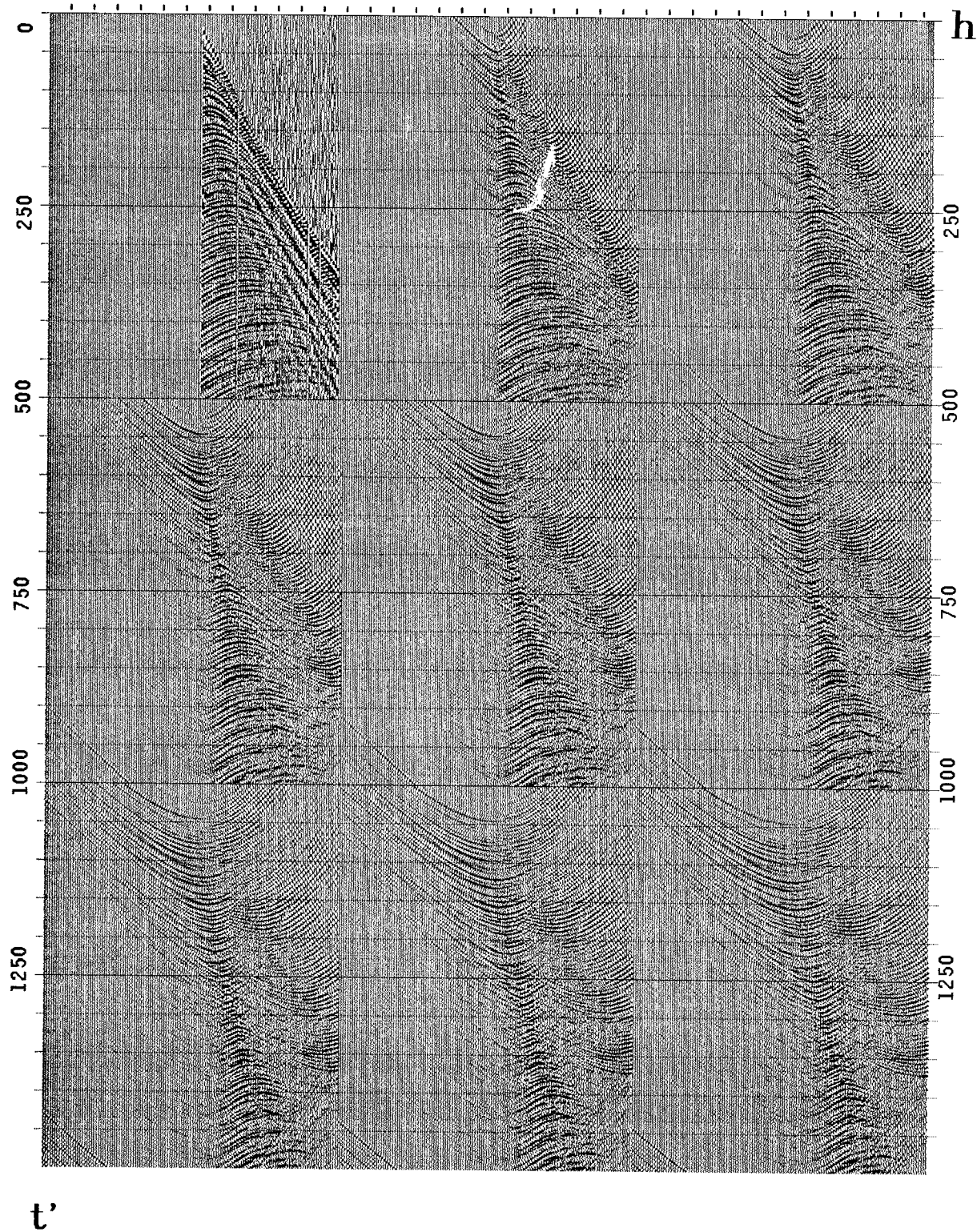FIGURE 3.2. (continuation).

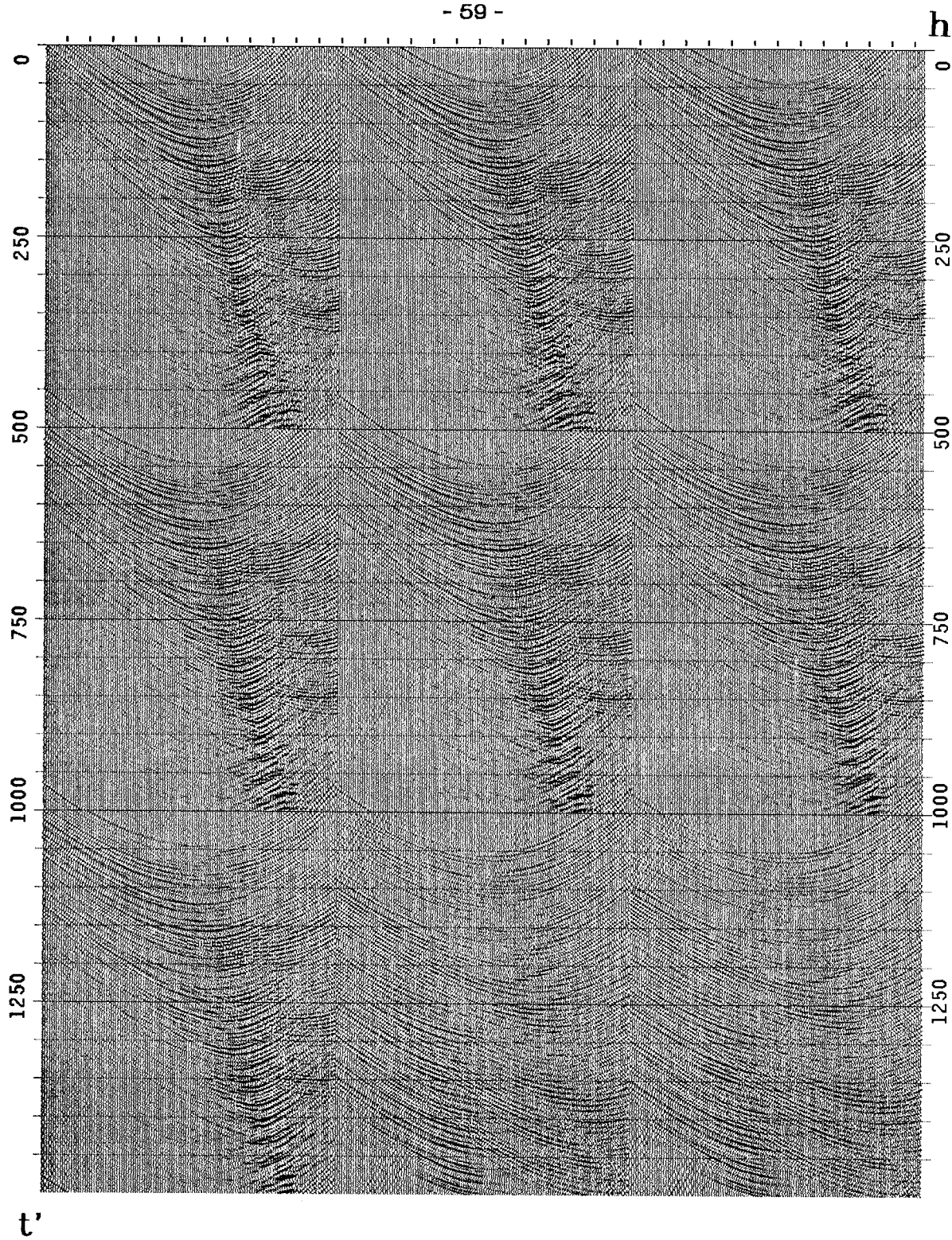FIGURE   . Downward continuation. $p_0 v = 0.3$.

FIGURE 3.3. (continuation).

imaged at each downward continuation step.

In figure (3.3) we have the slanted downward continuation situation. For a fixed reflector, energy migrates to the particular offset where the reference Snell wavefront reaches the surface. The LMO correction has the effect of an anti—alias filter. In the slanted frame there is less aliased energy moving in the wrong direction.

4.4. Wave equation velocity estimation.

Doherty and Clærbout (1976) introduced the wave equation to velocity estimation. The main idea was to downward continue the data to the depth of reflection. At this depth the offset coordinate should be independent of struc-ture, therefore better velocity estimates could be obtained. They also suggested velocity estimation in the $(h = 0, t, z)$ plane.

Yilmaz and Chambers (1981) using the wave equation defined a velocity spectrum with equations (3.1) and (3.4) for $p_0 = 0$ by letting velocity v be another variable in the representation:

$$f(h,\tau,t,v) = \frac{1}{4\pi^2} \int\int_{-\infty}^{\infty} F(k_h,\tau=0,\omega) \exp\left\{iT(v)\omega\tau + ik_hh - i\omega t\right\} dk_h \, d\omega$$

$$(4.1)$$

$$T(v) = 1 - \frac{1}{2}\left[1 - \left(\frac{k_hv}{2\omega}\right)^2\right]^{1/2}$$

$$(4.2)$$

Their *velocity spectrum* is the plane $f(h = 0, \tau, t = \tau, v)$

$$f(h=0,\tau,t=\tau,v) \;=\; \frac{1}{2\pi}\int\limits_{-\infty}^{\infty}\!\!\int F(k_h,\tau=0,\omega)\,\exp\left\{i(T(v)-1)\,\omega\,\tau\right\}dk_h\;d\omega$$

(4.3)

This equation is exact in constant velocity media. In this approach the wave equation stacks the data. The velocity spectrum obtained is similar to Taner and Koehler's (1968).

An alternative approach is to let the wave equation do NMO without stack. This was done by Thorson and Yedlin (1980), and Yedlin and Thorson (1981).

Clayton and McMechan (1981) used iterative wavefield inversion to estimate velocity using post—critical reflections and refraction data.

From chapter (I) we know the LMO method has several desirable properties over ray tracing methods of velocity estimation. Far offset data can be used for velocity estimation. Choice of p_0 can be done where the signal—to—noise ratio of the data is better. The method is linear. Multiple reflections preserve their timing relationships. However, the method itself does not define a suitable velocity spectrum; energy remains non—local. The LMO method can be applied at any depth of observation. At the surface of the earth, where data is collected, energy has been diffracted and is non—local. Using the wave equation in Snell midpoint coordinates, we can downward continue the seismic experiment to the depth and offset where the reference slanted wavefront was reflected. At this depth the data is imaged and no wave propagation has taken place. Imaging has the effect of stacking, not to zero offset, but to offsets where reference wavefronts with constant ray parameter p_0 reach the surface. This imaging step adds robustness to the LMO method in a sense of enhancing the signal—to—noise ratio. Cable truncation artifacts are not severe because imaging moves most of the

energy inside the data grid.

We define the *linear velocity spectrum* of a CMP gather as its image in Snell midpoint coordinates for a non—vertical reference wavefront. This definition fulfills the requirement that energy be a a local function of velocity. We analyze the resolution of our velocity spectrum while referencing downward continuation algorithms.

Choosing p_0. At some point in the process we need to decide what value of the ray parameter p_0 to use. A large p_0 implies wide propagation angles and increased velocity sensitivity for events with RMS velocity $v \approx 1/p_0$. However,
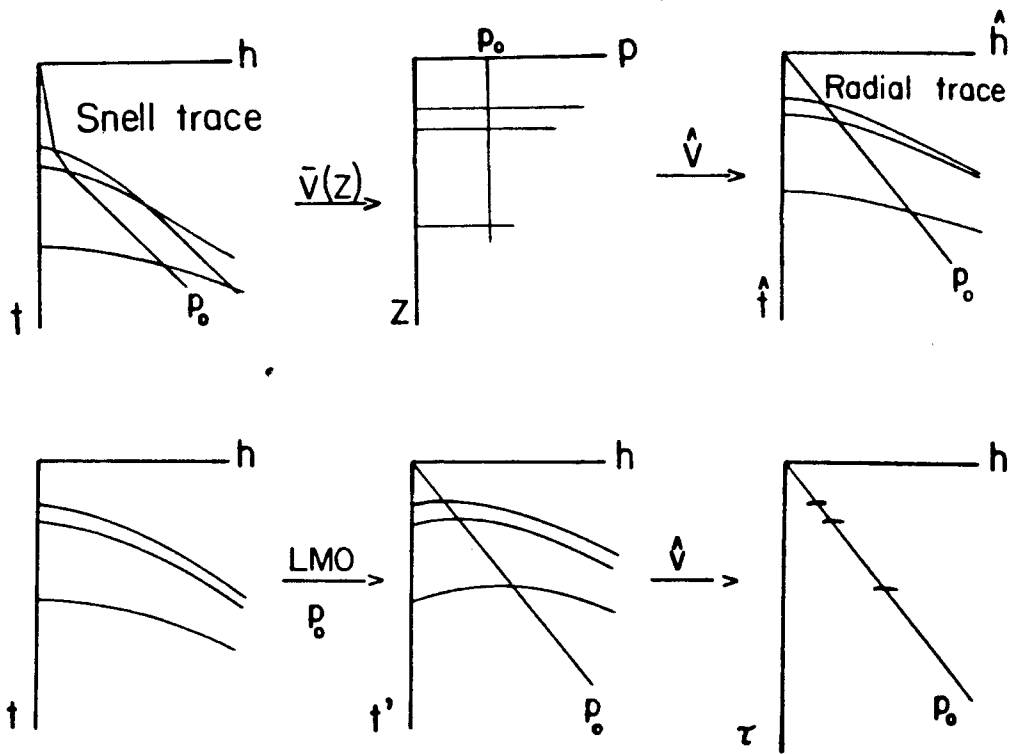

FIGURE 4.1. Iterative velocity estimation. Velocity estimation using Stolt imaging and hyperbolic stretch. The process consists of iteratively applying the two steps. Stolt imaging in Snell midpoint coordinates transforms the data into a space where we can read velocities directly from the imaged data. Hyperbolic stretch uses the current velocity function to map the data into a quasi—hyperbolic space. This space is more suitable for Stolt imaging.

with a large p_0 we cannot estimate high velocities ($v > 1/p_0$). Reference arrivals are beyond the end of the cable. Small p_0 will put low velocity events out of cable too, and since small propagation angles are used, there is a decrease in sensitivity to velocity. When wave equation imaging is used, to avoid severe end effects we also would like to keep a symmetry of positive and negative stepouts. Too small or too large p_0 will enhance the asymmetry of the skewed—hyperbolas in the data biasing velocity estimates. In practice we probably want to divide the data into several regions with different p_0 according to some rule; for instance

$$p_0 \approx [\, 0.5 - 0.8\,]/v_{max}$$

But no general rule can be given, the choice of p_0 is data dependent.

Phase shift method. (Appendix B). This method is exact up to Nyquist frequencies (wide angles) in stratified media. Exact methods are particularly sensitive to the downward continuation velocity, especially when trying to image wide angle energy. This sensitivity introduces two problems in our application. First, we can only expect to know *a priori* velocity with first order accuracy. Second, even if we know the correct velocity function, the phase shift method will only image primary energy. In some applications the velocity function is multivalued (multiples interfering with primaries), and we would like our velocity spectrum to give as good a resolution as possible for all velocities. The main application we have found for the phase shift method is studying downward continuation in Snell midpoint coordinates.

Stolt method. (Appendix C). Stolt's method has the advantage of speed. In a constant velocity medium the method is exact in the propagating region. For velocity estimation it is possible to reduce sensitivity to the background velocity,
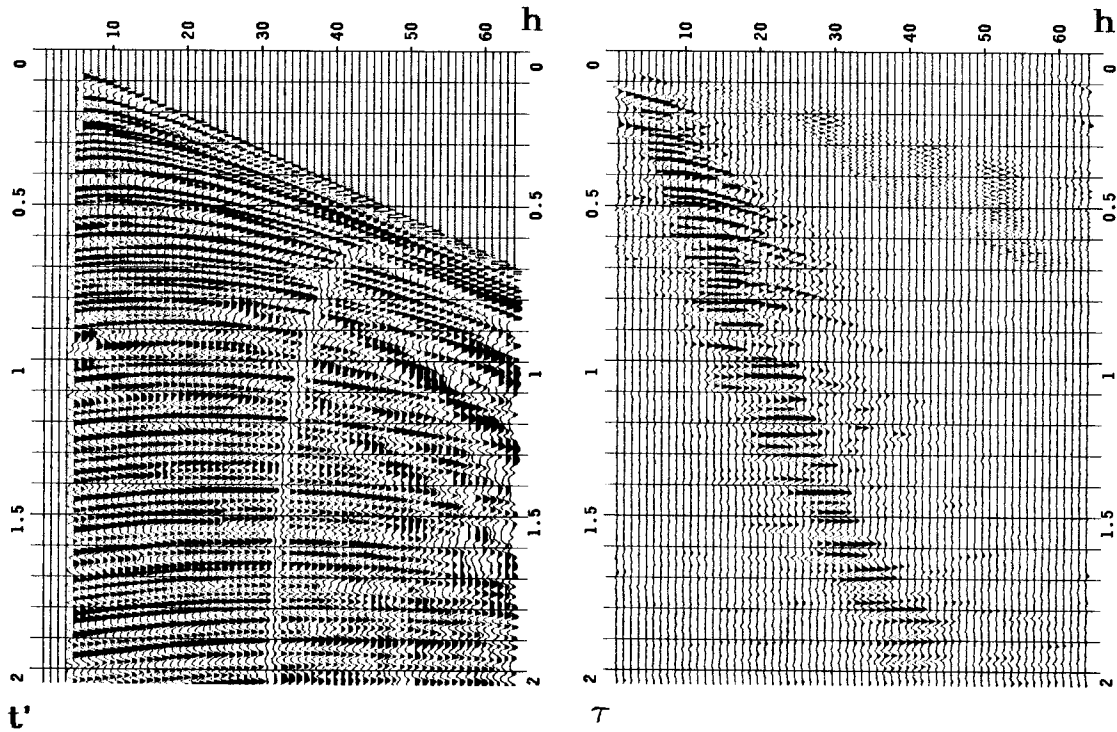
FIGURE 4.2. Imaged data in Snell coordinates. (a) Marine CMP gather in Snell midpoint coordinates after hyperbolic deformation. $\bar{v}(z)$ increases linearly with depth from the sea—floor to 1 km. ($\partial v / \partial z$ = 0.8 s^{-1}), (b) Stolt's image, amplitudes squared for display. Most events align along the replacement velocity slope $\hat{v}$ = 1700 m/s. With equation (4.7) we can correct the trial $\bar{v}(z)$ measuring departures from $\hat{v}$. This image defines our *linear velocity spectrum* — now energy is a local function of velocity. ($p_0\hat{v}$ = 0.255).

restricting the range of angles during the imaging step. Limiting the range of

angles also makes the method more insensitive to multivalued velocity functions

at the expense of blurred images. This is done, remembering that

$$H = \frac{k_h v}{2\omega} = \sin \vartheta'$$

When there are no multiple problems, we can decrease uncertainty in veloc-

ity by combining a deformation to hyperbolic space (chapter III) with Stolt's imag-

ing. We start imaging the data with constant velocity for a restricted range of

angles, and iterate decreasing the range as uncertainty in the velocity function

decreases. (Figure 4.1).

When we apply the iterative process, as the velocity function converges to the true one, Stolt's image aligns itself along the line associated with the background velocity $\hat{v}$ according to equation (I–3.16). We need a relation to correct the original $\bar{v}(z)$ from the observed departures of the image from $\hat{v}$.

Since from equation (I–3.3) there is a one–to–one relationship between velocity and the slope $d\tau/dh$ we can write an expansion for the velocity as function of m about $\hat{v}$

$$v = \hat{v} + \left[\frac{dv}{dm}\right]_{v=\hat{v}} \Delta m + \frac{1}{2!}\left[\frac{d^2v}{dm^2}\right]_{v=\hat{v}} (\Delta m)^2 + \cdots \qquad (4.4)$$

where m is equal to the slope $d\tau/dh$.

We can use equation (I–3.3) to find $\dfrac{dv}{dm}$

$$\left[\frac{dv}{dm}\right]_{v=\hat{v}} = -\frac{p_0}{4\left[p_0^2 + \dfrac{p_0}{2}m_{v=\hat{v}}\right]^{3/2}} \qquad (4.5)$$

We also have from equation (I–3.3) for $m_{v=\hat{v}}$

$$m_{v=\hat{v}} = 2\,\frac{1 - \hat{v}^2 p_0^2}{p_0\hat{v}^2} \qquad (4.6)$$

From these equations we can find the dv correction. Keeping the linear term only

$$dv_{v=\hat{v}} = \bar{v}_{v=\hat{v}} - \hat{v} = \left[\frac{dv}{dm}\right]_{v=\hat{v}} \Delta m = -\frac{p_0\hat{v}^3}{4}\Delta m \qquad (4.7)$$
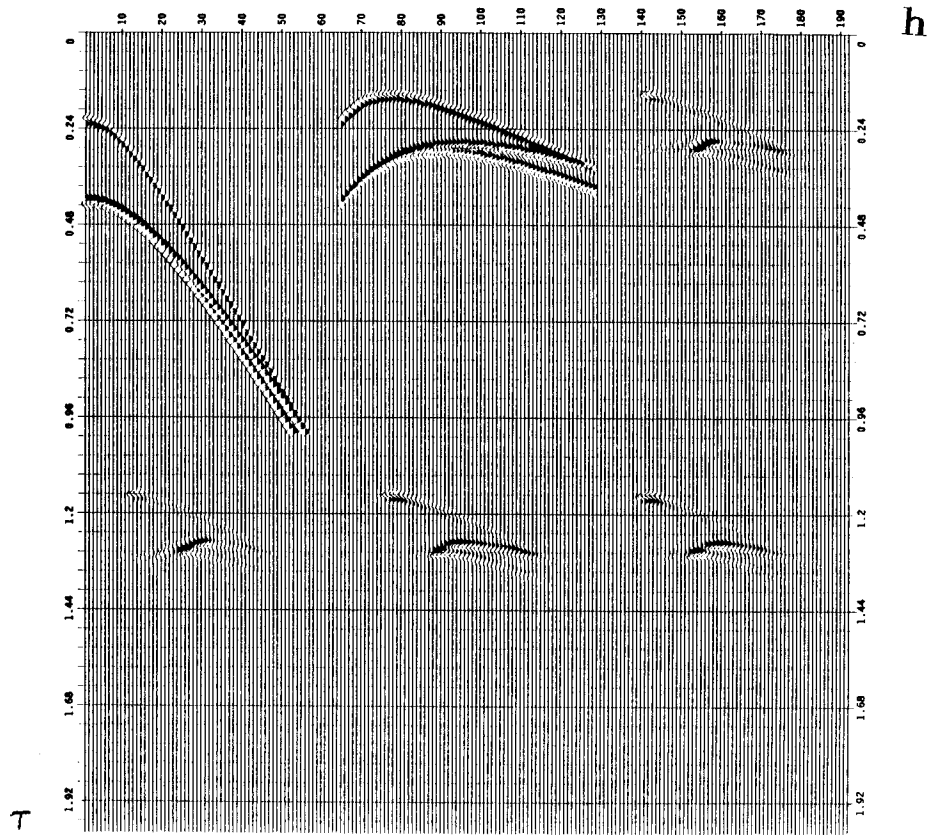
This is the desired relation.

FIGURE 4.3. Fifteen degree imaging. Narrow velocity spectrum. (a) Synthetic gather. $v_1 : v_2 : v_3 = 1 : 1 : 1.1$. (b) LMO corrected gather. $p_0 v_1 = 0.725$. (c) Constant velocity $p_0 \bar{v} = 0.80$ imaging. (d) $\bar{v}(h, \tau)$ imaging according to equation (4.9). Velocity was limited to the range $0.75 \leq p_0 \bar{v}(h, \tau) \leq 0.85$. (e) Same as (c) with $w_0 = 8\pi \sec^{-1}$. (f) Same as (d) with $w_0 = 8\pi \sec^{-1}$. Images have been squared for display. When trying to resolve narrow velocity variations, we want p_0 close to $1/v_{max}$, and small variations in the downward continuation velocity. Compare (c) with (d) and (e) with (f). There is a visible effect out of using $v(h, \tau)$, even though it varied only 6.25 % from the mean.

Figure (4.2) shows a field data example of the proposed iterative process. Data was preprocessed with a hyperbolic deformation and subsequently imaged with Stolt's method. In this figure another advantage of the LMO method can be seen, it is always possible to identify the events being used to measure velocity.
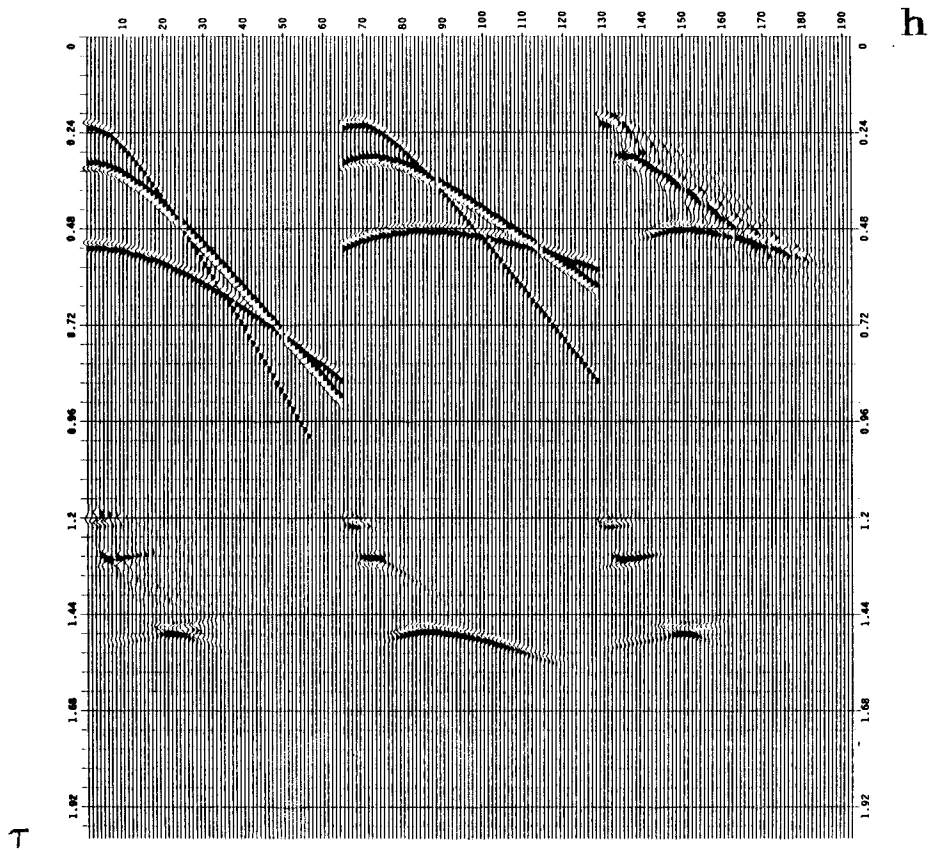
FIGURE 4.4. Fifteen degree imaging. Wide velocity spectrum. (a) Synthetic gather. $v_1 : v_2 : v_3 = 1 : 1.5 : 2$. (b) LMO corrected gather. $p_0 v_3 = 0.5$. (c) Constant velocity $p_0 \bar{v} = 0.35$ imaging. (d) $\bar{v}(h, \tau)$ imaging according to equation (4.9). Velocity was limited to the range $0.175 \le p_0 \bar{v}(h, \tau) \le 0.525$. (e) Same as (c) with $w_0 = 8\pi \sec^{-1}$. (f) Same as (d) with $w_0 = 8\pi \sec^{-1}$. Images have been squared for display. $v(h, \tau)$ has a broad range of variation for this application. We get a sharper image when using inhomogeneous instead of constant downward continuation velocity.

Finite difference in (h, τ, ω) **domain.** (Appendix D). Imaging CMP gathers in Snell midpoint coordinates has the useful feature of separating energy with respect to angle. Multiple reflections stay aligned below their associated primaries (at water velocity slope), becoming easier to discriminate. Refractions remain at high angles and do not interfere too strongly with primaries. We would like to exploit this feature in our velocity spectrum.

Fifteen degree finite difference algorithms in (h, τ, ω) space have several advantages. Time derivatives are exact. The fifteen degree equation is insensitive to background velocity within small propagation angles (departures measured from the reference Snell wave propagation angle). In this domain, stepout filtering concurrent with downward continuation is also possible. (Appendix D).

Since our equations are now in offset space, the possibility of allowing variations of velocity with offset is open. This may help contravene numerical dispersion errors. More important, from equation (I-3.3) we know that Snell wave arrival positions are function of velocity. For a fixed τ we expect to see low velocity arrivals at offsets smaller than fast velocity arrivals. Keeping in mind that the fifteen degree approximation correctly images the Fresnel zone of a given reflection, it should be able to handle multi-valued velocity functions. When there are two simultaneous arrivals at zero offset in the data, we should be able to focus both events if the Fresnel zone of both reflectors decouples within cable boundaries at large offsets. We could then use low velocities at small offsets and high velocities at large offsets. When chosing p_0 these arguments should be kept in mind. Energy outside the Fresnel zone can be filtered out.

The fifteen degree equation in Snell midpoint coordinates is given by

$$\frac{\partial}{\partial \tau} f(h,\tau,\omega) = \frac{v(h,\tau)^2}{8(w_0 - i\omega)\,[1 - p_0^2 v(h,\tau)^2]}\, \frac{\partial^2}{\partial h^2} f(h,\tau,\omega) \qquad (4.8)$$

where w_0 is the stepout filtering parameter.

For a choice of $v(h, \tau)$ we can use equation (I-3.3) as

$$v^2(h, \tau) = \frac{1}{p_0 \left[p_0 + \dfrac{1}{2}\dfrac{\tau}{h} \right]} \qquad (4.9)$$

Figure (I—3.2) shows how this equation dictates the velocity distribution in (h, τ) space.

In the fifteen degree equation (4.8) $v(h, \tau)$ is expected to be an interval velocity, while equation (4.9) defines RMS velocities. The fifteen degree equation is insensitive to this distinction. To justify the use of equation (4.9), consider an event at time—depth τ. We need to extrapolate τ sec to reach the depth of the event. Assuming only τ dependence in velocity*, the coefficient of equation (4.8) from its finite difference scheme is

$$a(\tau) \equiv \frac{v^2(\tau)\Delta\tau}{16\,\omega[\,1 - p_0^2\,v^2(\tau)\,]\Delta h^2} \tag{4.10}$$

The cumulative effect of downward continuation is given by the integral

$$\int_0^\tau a(\xi)\,d\xi = \frac{1}{16\,\omega\Delta h^2}\int_0^\tau \frac{v^2(\xi)}{1 - p_0^2\,v^2(\xi)}d\xi \tag{4.11}$$

we recognize the v_{RMS} expression of equation (I—3.13); define $\bar{a}$ as

$$\bar{a} \equiv \int_0^\tau a(\xi)\,d\xi = \frac{\tau}{16\,\omega\Delta h^2}\frac{v_{RMS}^2}{1 - p_0^2\,v_{RMS}^2} \tag{4.12}$$

Therefore with the fifteen degree equation there is no difference in extrapolating a single τ step with $\bar{a}$ or extrapolating continuously with $a(\tau)$. This insensitivity was exploited to estimate velocity in the $(h = 0, t, z)$ plane for $p_0 = 0$ by Doherty and Claerbout (1974). Unfortunately their analysis cannot be extended to $p_0 \neq 0$. The plane $(h = h_0, t, z)$ where energy focuses is velocity dependent. In addition, this plane is non—unique when velocity is multivalued.

---

*In the neighborhood where the fifteen degree wave equation is valid $v(h, \tau) \approx v(\tau)$.
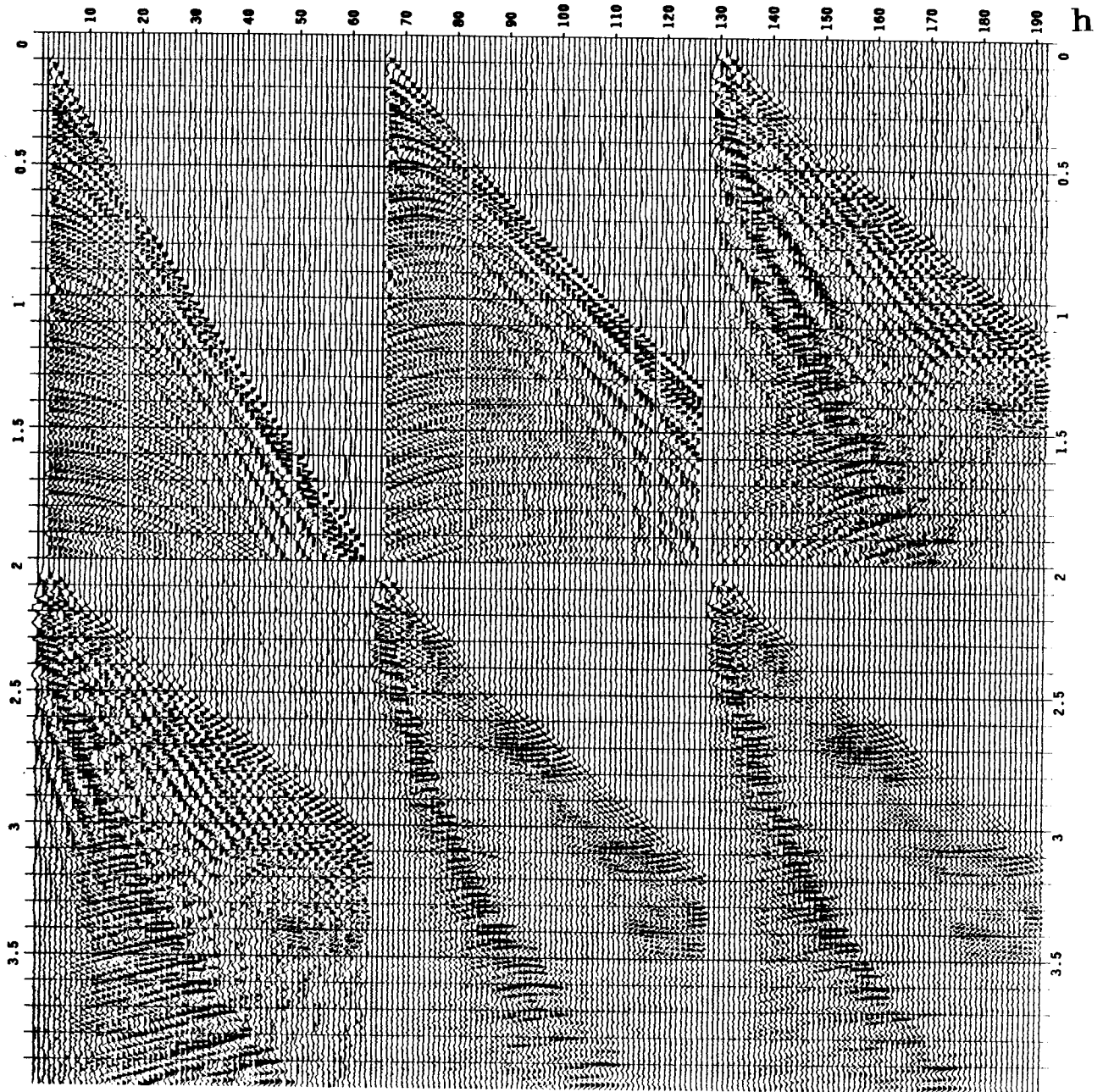
FIGURE 4.5. Fifteen degree imaging. Field data. Wide velocity spectrum. (a) CMP gather. (b) LMO gather $p_0 = 1/5000\ sec/m$. (c) Constant velocity imaging. $\bar{v} = 2000\ m/sec$. (d) $v(h,\tau)$ imaging. Velocity was allowed to vary with offset according to equation (4.9) in the range $1200\ m/sec \le \bar{v} \le 2800\ m/sec$. (e) Same as (c) with $w_0 = 8\pi\ sec^{-1}$. (f) Same as (d) with $w_0 = 8\pi\ sec^{-1}$. This data set has strong multiple refractions that give strong interference with the image in both constant and variable velocity imaging. With constant velocity imaging the image is not well defined for the first second of data. Variable velocity defines it better. However variable velocity has strong unmigrated high stepout events in the low velocity zone. With stepout filtering is added, the quality of the image is slightly better when $v(h,\tau)$ was used.

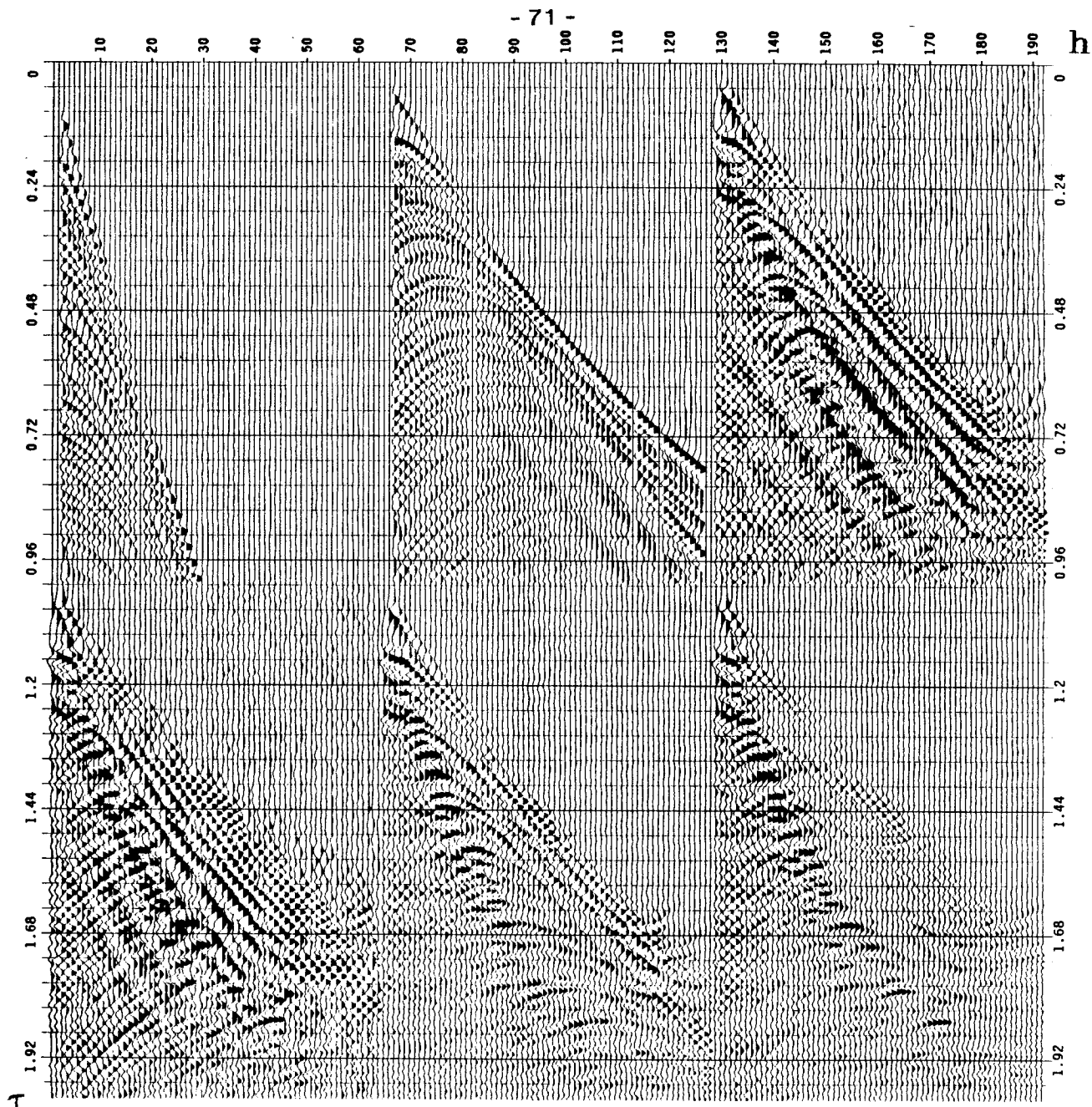FIGURE 4.6. Fifteen degree imaging. Field data. Narrow velocity spectrum. (a) CMP gather. (b) LMO gather $p_0 = 1/2667\ sec/m$. (c) Constant velocity imaging. $\bar{v} = 1800\ m/sec$. (d) $v(h, \tau)$ imaging. Velocity was allowed to vary with offset according to equation (4.9) in the range $1400\ m/sec \le \bar{v} \le 2200\ m/sec$. (e) Same as (c) with $w_0 = 8\pi\ sec^{-1}$. (f) Same as (d) with $w_0 = 8\pi\ sec^{-1}$. For this window of data, multiple refractions interfere severly with the image of the data. Imaging without numerical viscosity does not give good resolution. Stepout filtering and $v(h, \tau)$ improve the image quality. In (f) the spectrum has resolved peg—leg multiples aligned at water slope. They image below primary arrivals.

Figure (4.3) is an example of imaging to resolve two simultaneous arrivals. The synthetic shows two events with RMS velocities differing by 5%. The reference ray parameter should be chosen so the stationary region of LMO corrected events separates according to velocity. We also need to restrict the range of variation of the downward continuation velocity. The figure illustrates a problem trying to get an image with large p_0. When the energy distribution is not symmetric with stepout, the maximum cluster of energy will migrate as downward continuation proceeds. When imaging, the maximum—energy locations will not necessarily coincide with the stationary location of events, this can result in a bias estimating velocity. Stepout filtering partially solves this problem.

Figure (4.4) is an example of imaging to resolve wide velocity variations. In this application the range of variations of $v(h, \tau)$ is broader than in the previous example. Imaging gives a sharper focus when $v(h, \tau)$ is used instead of constant downward continuation velocity.

Figure (4.5) is an example with field data. The spectrum is obtained for two seconds of data. The data set has particularly strong multiple refractions. The image illustrates how the LMO method separates events with velocity. Refractions remain at large offsets and can easily be removed with stepout filtering, this way they will not interfere in the velocity estimation process. Figure (4.6) is the example with the first second of data. The filtered image is better when $v(h, \tau)$ is used. Some peg—leg multiples have been resolved.

The image data contains several focused events that are not distinguishable in the original diffracted data. A convenient way to study the source of focused energy is with a movie displaying downward continuation and imaging simultaneously. Figures (4.7) and (4.8) display some of the movie frames. Each frame has been downward continued a given $\Delta\tau$ step replacing downward continued data

with their image after reaching their corresponding time–depth τ. As downward continuation proceeds the high stepout energy from the multiple reflected refractions was attenuated numerically so it does not interfere with reflected energy images. In the diffracted data it is difficult to identify the stationary zones of hyperboloids corresponding to multiple energy. Following the downward continuation it is possible to see how events separate. This data set has strong peg–leg multiples that have been separated and focused from the primaries. (Peg–leg multiples align at water velocity slope below their associated primary). $v(h,\tau)$ imaging gives better separation than constant velocity imaging.
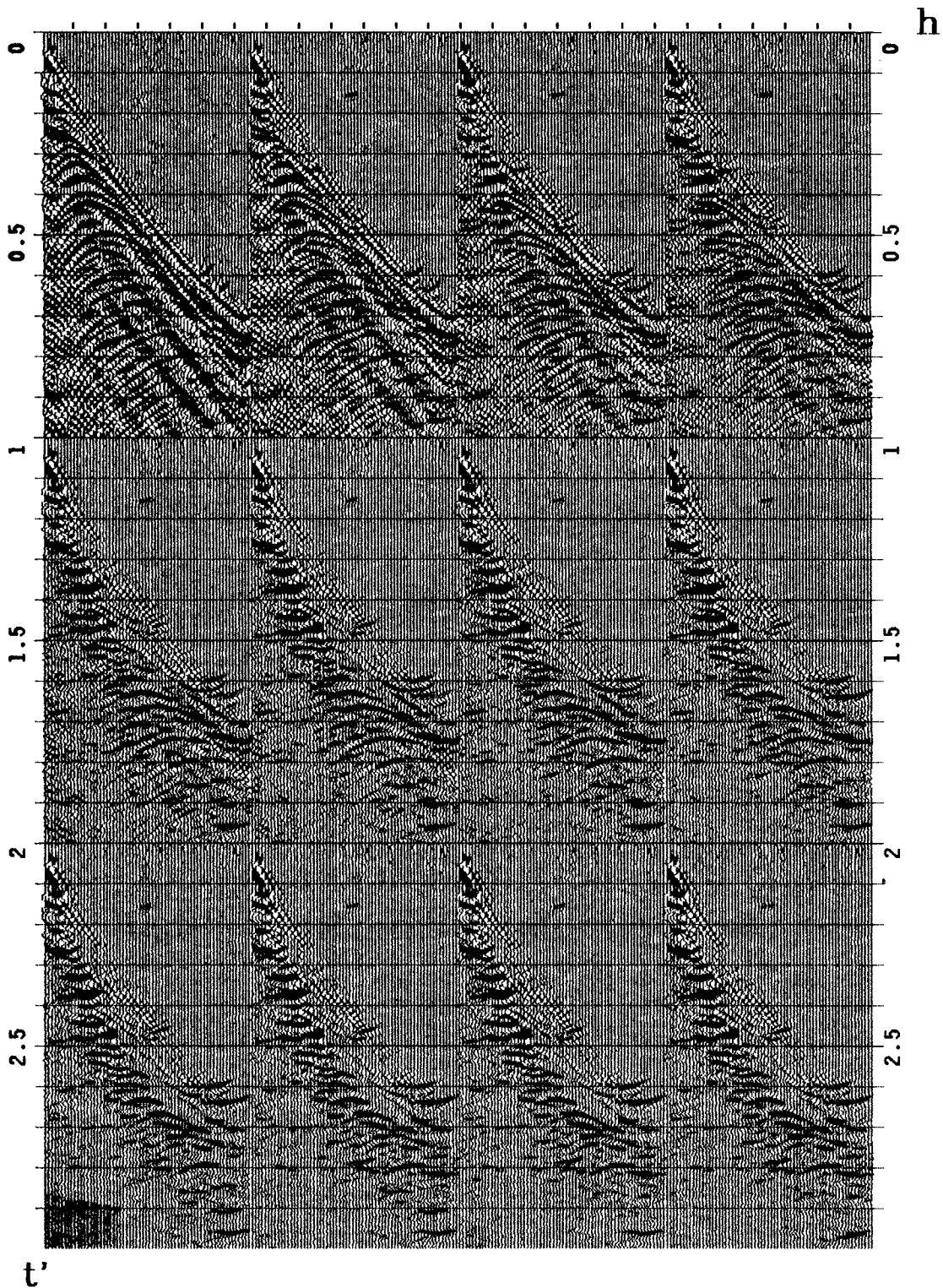
FIGURE 4.7. Downward continuation and imaging. Constant velocity. Each panel displays downward continued and imaged data at $\Delta\tau \approx 0.084\,sec.$ increments. Downward continued data is replaced by its image when its time—depth τ is reached. Following the downward continuation makes it easier to identify the source diffraction of focused energy. In the original diffracted data it is difficult to separate primary energy from sea—floor and peg—leg multiples. During imaging, multiple reflected refractions are filtered out so they do not interfere with reflection images. The final image has separated several peg—leg multiples undistinguishable in the diffracted data. LMO: $p_0 = 1/2500\,sec/m$. Constant velocity $v = 1800\,m/sec$ imaging. $w_0 = 8\,\pi\,sec^{-1}$.
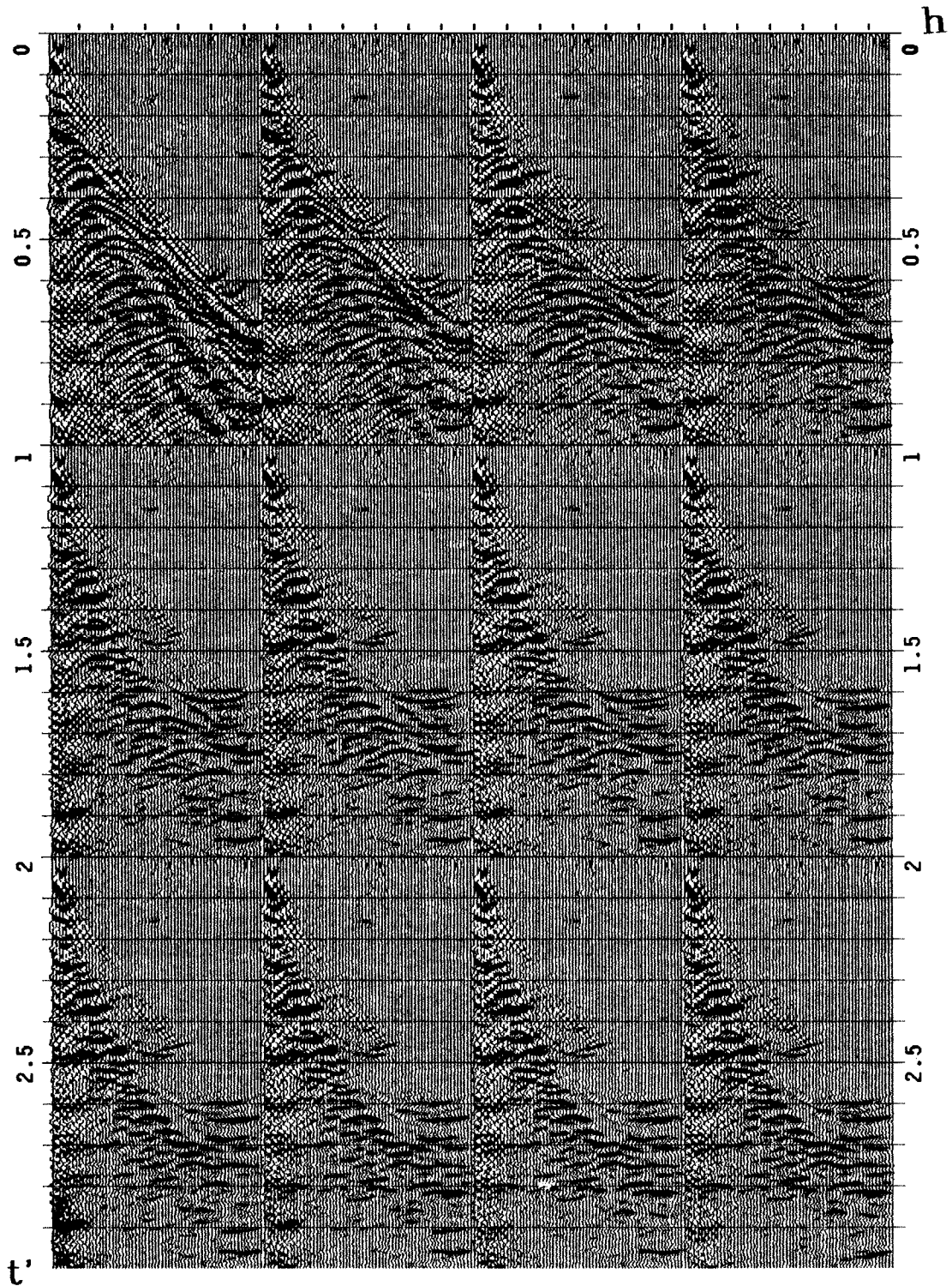
FIGURE 4.8. Downward continuation and imaging. $v(h,\tau)$. This figure is similar to Figure (4.7) using $v(h,\tau)$. For near offsets the velocity is low so we cannot get a good image. In the far offsets there is some improvement in imaging. There is better separation between primary and multiple energy compared to constant velocity imaging. LMO: $p_0 = 1/2500\ sec/m$. $v(h,\tau)$ imaging; velocity allowed to vary with offset according to equation (4.9) in the range $1400\ m/sec \leq \bar{v} \leq 2200\ m/sec$. $w_0 = 8\pi\ sec^{-1}$.